

**Epitaxial lateral overgrowth of tin spheres driven and directly observed  
by helium ion microscopy**

Klingner, N.; Heinig, K.-H.; Tucholski, D.; Möller, W.; Hübner, R.; Bischoff, L.;  
Hlawacek, G.; Facsko, S.;

Originally published:

September 2022

**Journal of Physical Chemistry Letters 126(2022), 16332-16340**

DOI: <https://doi.org/10.1021/acs.jpcc.2c03707>

Perma-Link to Publication Repository of HZDR:

<https://www.hzdr.de/publications/Publ-34525>

Release of the secondary publication  
on the basis of the German Copyright Law § 38 Section 4.

# Epitaxial lateral overgrowth of tin spheres driven and directly observed by helium ion microscopy

Nico Klingner\* Karl-Heinz Heinig David Tucholski Wolfhard Möller René Hübner Lothar Bischoff Gregor Hlawacek Stefan Facsko

Dr. Nico Klingner, Dr. Karl-Heinz Heinig, David Tucholski, Prof. Dr. Wolfhard Möller, Dr. René Hübner, Dr. Lothar Bischoff, Dr. Gregor Hlawacek, Dr. Stefan Facsko  
Helmholtz—Zentrum Dresden—Rossendorf e.V.,  
Bautzner Landstr. 400, 01328 Dresden, Germany  
Email Address: n.klingner@hzdr.de

Keywords: *helium ion microscope, tin whisker growth, defect kinetics*

Enhanced interstitial diffusion in tin is a phenomenon often observed during ion-beam irradiation and in lead-free solders. For the latter, this not very well understood, strain-driven mechanism, results in the growth of whiskers which can lead to unwanted shorts in electronic designs. In ion-beam physics, this phenomenon is often observed as a result of the enhanced formation of Frenkel pairs in the energetic collision cascade. Here, we show how epitaxial growth of tin extrusion on tin-oxide-covered tin spheres can be induced and simultaneously observed by implanting helium using a helium ion microscope. Calculations of collision cascades based on the binary collision approximation and 3D-lattice-kinetic Monte Carlo simulations show that the implanted helium will occupy vacancy sites, leading to a tin interstitial excess. Sputtering and phase separation of the tin oxide skin—which is impermeable for tin atoms—creates holes and will allow the epitaxial overgrowth to start. Simultaneously, helium accumulates inside the irradiated tin sphere and builds up additional strain. Fitting the simulations to the experimentally observed morphology allows us to estimate the interface energy between tin and tin oxide to  $1.98 \text{ J m}^{-2}$ . Our approach allows the targeted initiation and in-situ observation of interstitial-diffusion-driven effects to improve the understanding of the tin-whisker growth mechanism observed in lead-free solders.

## 1 Introduction

The growth of tin whiskers has been extensively studied over the last 70 years and has increased even more in recent years due to the ban on lead-containing solder [1, 2]. One reason is that alternative solder formulations are prone to whisker formation [3, 4]. The detailed mechanisms of whisker growth are still under discussion, especially the source of point defects and their kinetics [5–7]. At room temperature, tin whisker growth takes

weeks or even months, which makes experimental studies time-consuming. Point defect creation by ion irradiation can accelerate the kinetics of the growth of extrusions considerably. On the other hand, high-fluence helium implantation into semiconductor materials and metals causes bubble and blister formation [8–13], serving valuable insights for first wall fusion reactor materials research [14]. Furthermore, ion irradiation of nano-objects can considerably change their shape due to mechanisms like ion-beam hammering [15], ion-induced shaping of buried particles [16], or ion-induced viscous flow of nanopillars [17]. These shape changes are mainly driven by the kinetics of defects generated by collisions of atoms with energetic ions and recoils. Defect generation by electron irradiation can also cause shape changes of nanoobjects [18]. Here, we report on an interesting observation during medium-fluence  $\text{He}^+$  irradiation of micrometer-sized tin spheres. The experiments were carried out with gas-field-ion-source (GFIS) based focused  $\text{He}^+$  irradiation using helium ion microscopy (HIM). This approach enables the in-situ observation of the ion-induced shape transformation of Sn micro-spheres with sufficiently high resolution. To explain the observed shape changes, one needs to consider He implantation into the Sn micro-spheres causing ion-beam mixing and the production of Frenkel pairs as well as the subsequent He nano-bubble formation. To better understand the  $\text{He}^+$ -irradiation-induced morphology changes of Sn spheres caused by the kinetics of point defects (He-interstitials, tin interstitials and tin vacancies), we have developed an appropriate diffusion-reaction model and employed 3D-lattice-kinetic Monte Carlo (3DlkMC) simulations. These simulations provide detailed information on the mechanisms of the nucleation and growth of the observed Sn extrusion. It is shown that the growth starts at holes in the  $\text{SnO}$  skin of the spheres formed by ion erosion, followed by epitaxial lateral overgrowth (ELO) fed by Sn interstitials coming from the interior of the Sn spheres. The presented combination of experimental studies and atomistic simulations will improve the understanding of point defect kinetics in tin, which controls the whisker growth too.

## 2 Experimental Results

The experiments were performed with tin spheres on a carbon substrate—a widely used standard for scanning electron microscopy (SEM) and manufactured by vapor deposition [19]. Tin has very low wettability on the carbon substrate and forms, due to its high surface tension, almost perfect spheres with sizes ranging from a few nanometers to several tens of micrometers. This type of sample allows an easy and fast inspection and correction of astigmatism over a wide magnification range in SEM, focused ion beam (FIB), or HIM devices. Commercially, the tin sphere standard is available from various suppliers [20–22]. The sample used in our experiments was purchased from [23], specified to particle sizes from 5 nm to 30  $\mu\text{m}$ .

The ion-beam exposure of the tin spheres was performed with a helium ion microscope. HIM is well known for imaging, modification, as well as for material analysis on the nanometer scale [24–29]. It is best suited to perform a local He or Ne exposure with a very high fluence due to the beam spot size smaller than 1 nm and the possibility of in-situ observation of the irradiated area using the same beam. The irradiation was performed by scanning the beam in line-by-line mode over a small subset of tin spheres. The so-obtained high-resolution images of the nanostructures were then analyzed with respect to the observed geometric changes of the tin spheres. The fluence typically applied per image was chosen to be below  $1 \times 10^{16}$  ions  $\text{cm}^{-2}$  to track small ion-induced modifications.

In **Figure 1**, snapshots of a typical irradiation with 28 keV helium ions are shown. After a homogeneously distributed fluence of  $2 \times 10^{17}$  ions  $\text{cm}^{-2}$ , small pyramidal extrusions form preferentially at the equator of the irradiated spheres, where the north pole points to the ion source (Figure 1b). With increasing fluence, these extrusions become bigger in size and begin to overgrow the surface (Figure 1c). Later on, the extrusions become more and more faceted (Figure 1d to 1h). In Figure 1h, a larger field of view (FOV) including parts of the non-irradiated surface is presented. Extrusions from tin spheres form only in the irradiated area or only a few tens of nanometers from its rim. Above a fluence of  $5 \times 10^{17}$  to  $7 \times 10^{17}$  ions  $\text{cm}^{-2}$ , helium bubbles seem to emerge on the surface. The collapsed surface locations are indicated by blue arrows in Figure 1f and Figure 1g. Once this fluence is exceeded, no further extrusion growth was ob-

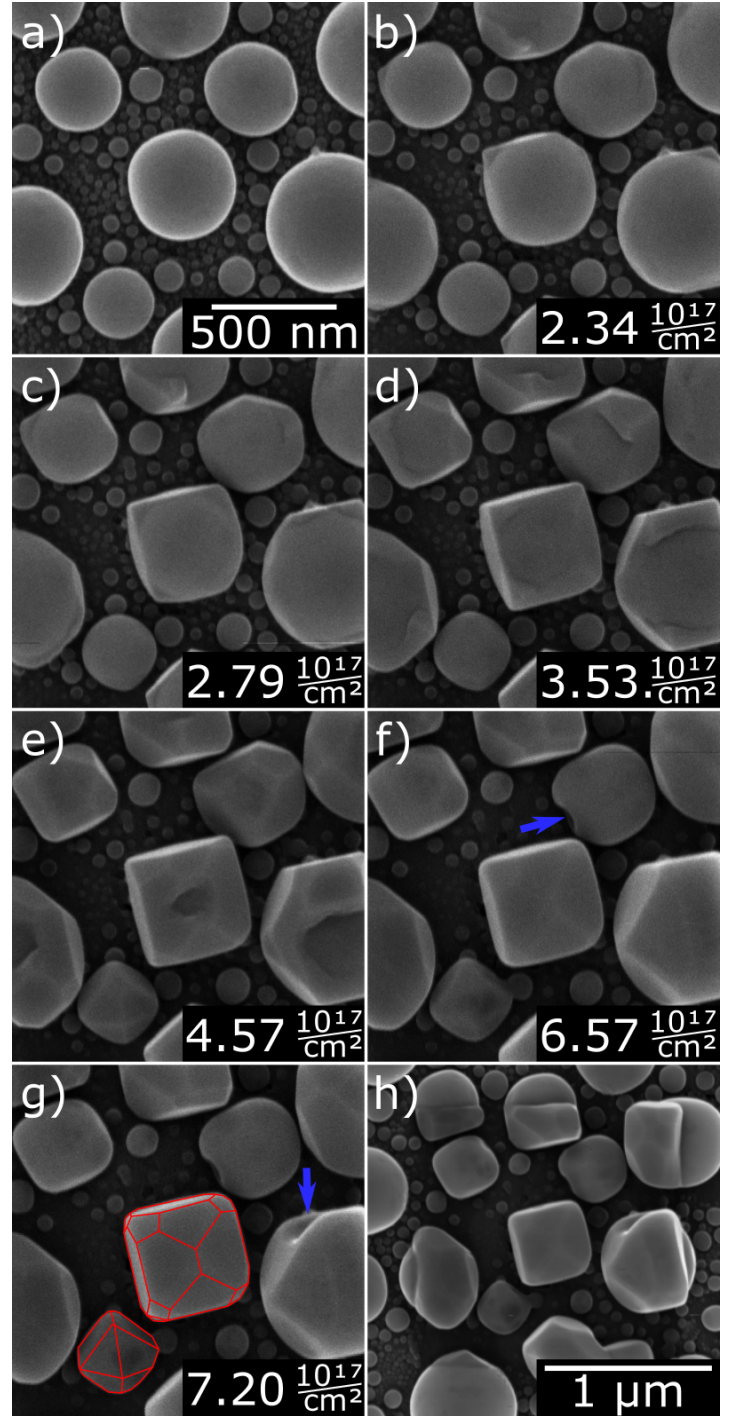


Figure 1: HIM images of a) pristine, not irradiated tin spheres on carbon sample. b) to g) same sample region after the irradiation of various fluences as indicated in the images. Field of view (FOV) of a) to g) is 1.4  $\mu\text{m}$  (cropped from 2.0  $\mu\text{m}$ ). h) Image of the irradiated area captured on a larger FOV of 2.2  $\mu\text{m}$  (cropped from 4.0  $\mu\text{m}$ ). No morphological changes of the tin spheres are visible outside the irradiated area. Collapsed bubbles are indicated by blue arrows in f) and g).

served on these spheres and the edges of the facets become rounded.

Images of several irradiation experiments were recorded as videos and can be found in the supplementary information. The noise-level of the videos was improved by a recursive prediction/correction algorithm based on the Kalman-Filter [30].

Irradiations with various beam parameters were performed. Primary ion energies from 10 to 30 keV, ion currents from 0.1 to 8 pA and different FOV from 0.6 to 4  $\mu\text{m}$  were adjusted—all  $\text{He}^+$  irradiations led to the described phenomena with only slight variations. Tin spheres smaller than about 150 nm do not show any extrusion, they only shrink due to erosion by ion sputtering. Simulations with the TRIM program [31] show that the projected  $\text{He}^+$  range at 30 keV is  $(149 \pm 67)$  nm, which coincides with the threshold radius of the smallest spheres forming extrusions, which was determined to be  $(150 \pm 50)$  nm for 28 keV helium ions.

We did not observe any flux dependence within the range of  $2.6 \times 10^{13}$  to  $4.1 \times 10^{15}$  ions  $\text{cm}^{-2} \text{s}^{-1}$ . Once extrusions are formed, they are stable over time and grow, provided they are not destroyed by emanating He bubbles or sputtering due to continuous  $\text{He}^+$  ion irradiation.

A similar tin sphere evolution was observed under  $\text{Ne}^+$  ion irradiation in the HIM, but the extrusions formed were much smaller in size before the process stopped due to neon gas bubbles reaching the particle surface (not shown here).

A large tin sphere with a diameter of 4.7  $\mu\text{m}$  has been irradiated only partly in an area of 2  $\mu\text{m} \times 2 \mu\text{m}$ . In **Figure 2**, snapshots from the irradiation are shown. In Figure 2a, extrusions are not yet visible on the large sphere, while the smaller one at the right edge of the image already shows clear facets. In Figure 2b, a small extrusion becomes visible at the equator of the large sphere, where the ion beam hits the surface nearly tangentially. The small extrusion grows slowly with increasing fluence, see Figure 2c. In Figure 2d, a second extrusion with an equal-facet orientation appears close to the first one. In Figure 2e, both extrusions have merged into a larger one. Gaps between both extrusions have been filled and show clear merged facets keeping the initial orientation, and the extrusions on the smaller spheres start rounding. The final size of the described extrusions on the sphere on the bottom right side of the image is nearly reached in Figure 2f. In contrast to

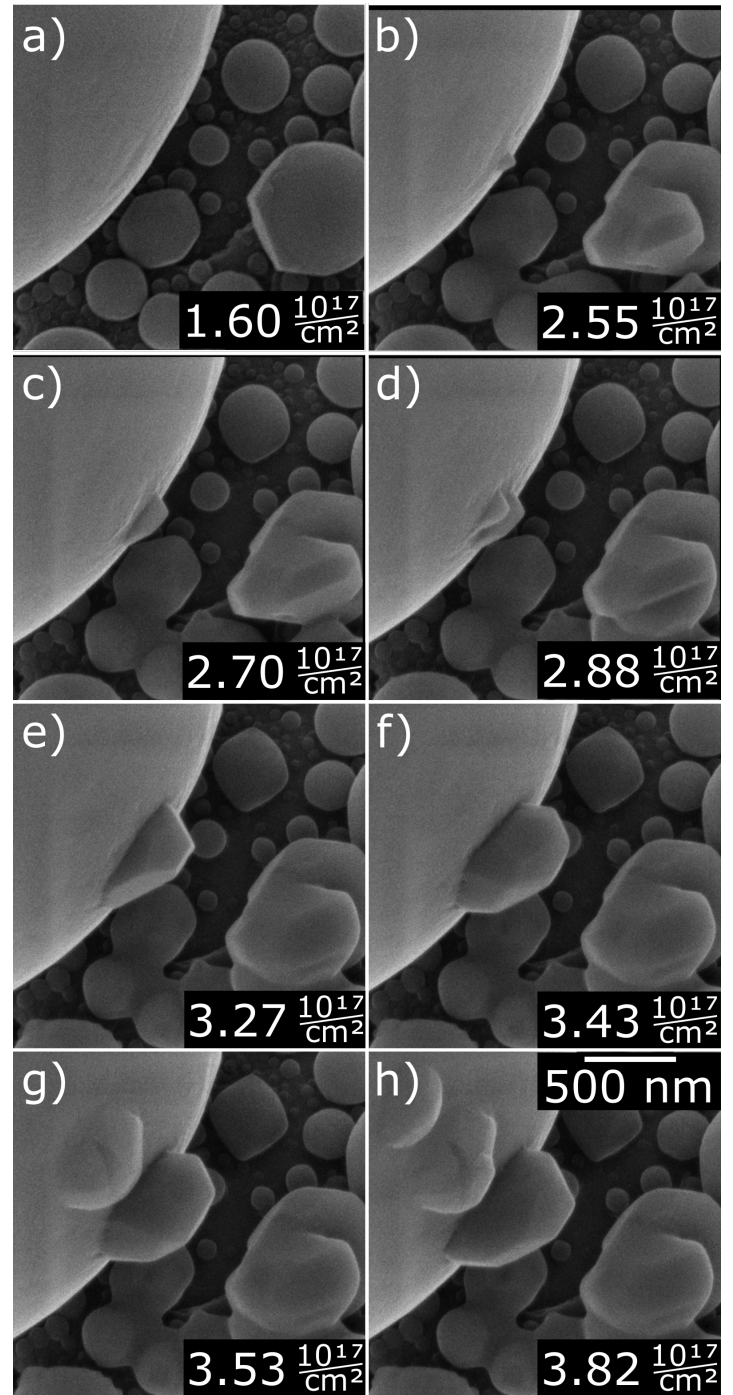


Figure 2: a) to h) HIM snapshots of the irradiation of tin spheres for increasing fluencies. A partially irradiated larger tin sphere with a diameter of around 4.7  $\mu\text{m}$  can be seen in the top left corner. The field of view is 1.9  $\mu\text{m}$  cropped from an irradiated area of 2.0  $\mu\text{m}$ .



the growth of the crystal-like facets in Figures 2a to 2f, the extrusion appearing in Figure 2g has a more rounded bubble-like shape. This feature is popping up within just two consecutive single image scans equivalent to a fluence difference of only  $7 \times 10^{14}$  ions  $\text{cm}^{-2}$ . Finally, after  $3.82 \times 10^{17}$  ions  $\text{cm}^{-2}$  (see Figure 2h), another more spherical extrusion appears above the older extrusions after only a small amount of additional fluence. The process seems to be different for the extrusions appearing in Figures 2a to 2f than for the features showing up in Figures 2g and 2h. For a better presentation of the evolution of the extrusions, the process can be seen as a movie in the supplementary information.

For transmission electron microscopy (TEM) analysis, pristine tin spheres were mechanically removed from the surface onto carbon-coated copper grids. In the high-resolution transmission electron microscopy (HRTEM) images presented in **Figures 3a** and 3b, the crystallinity of a 80 nm small unirradiated tin sphere passivated by a 3 to 5 nm oxide layer is visible. While the spheres possess the well-known single-crystalline tetragonal  $\beta$ -tin structure (Figure 3a to 3c), the amorphous outer shell layer was proven to be a Sn oxide using energy-dispersive X-ray spectroscopy (EDXS) analysis (not shown here). Additional X-ray photoelectron spectroscopy (XPS) analysis confirmed a tin-to-oxygen ratio of 47 to 53 at %. We therefore conclude that the layer consists of meta-stable tin(II) oxide SnO (stannous oxide). We assume that this oxide layer is a native oxide layer that forms under air exposure and that it covers all tin spheres homogeneously [32].

In Figure 3d, a HIM image of a tin sphere is presented that was irradiated with a fluence of  $2.4 \times 10^{17}$  ions  $\text{cm}^{-2}$ . The growth of several extrusions on the equator of the sphere was monitored during the helium irradiation process. The irradiation was stopped after the first extrusions appeared to later obtain TEM images of this stage in the formation process.

The crystal orientation of all extrusions was investigated by TEM analysis. A TEM image of the extrusion indicated in Figure 3d is presented in Figure 3e. Selected-area electron diffraction analysis of all extrusions and the tin spheres show identical diffraction patterns, which can be indexed with the  $\beta$ -Sn structure (Figure 3f). This result gives a strong evidence that the tin sphere is mono-

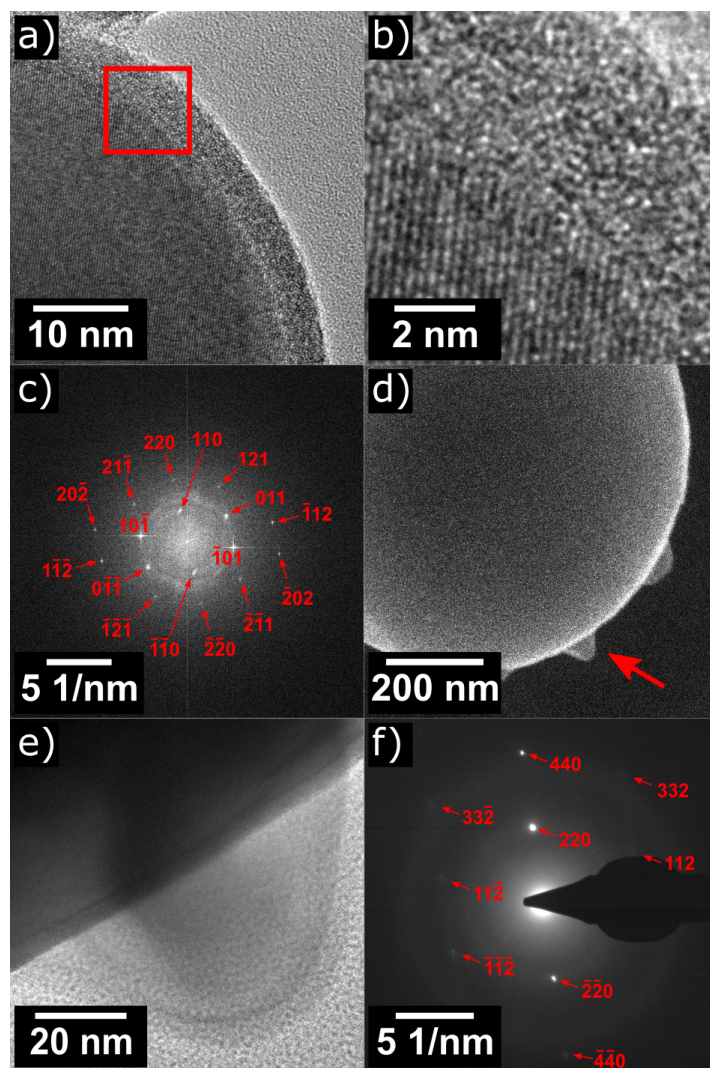


Figure 3: a) HRTEM image of a small, pristine tin sphere (FOV 37.9 nm); the square indicates the area that is shown at higher magnification in b). c) Fast Fourier transform of a HRTEM image (FOV of 37.9 nm) of the inner crystalline part of the tin sphere shown in a). Indexing was done based on the  $\beta$ -tin structure in  $\bar{1}1\bar{1}$  zone axis geometry. d) HIM image of irradiated sphere on a carbon-coated TEM grid, e) overgrown crystalline extrusion, indicated by an arrow in d). f) Selected-area electron diffraction pattern of the extrusion shown in d). Indexing was done based on the  $\beta$ -tin structure in  $\bar{1}10$  zone axis geometry.

crystalline and that the extrusion have grown epitaxially.

The tin spheres were also analyzed after gallium FIB cross-sectioning to gain information on the internal structure. For this purpose, unirradiated and irradiated spheres were cut in half with a Ga-FIB, and the resulting cross-sections were imaged at 54° tilt using SEM (see **Figure 4**). The internal structure of an unirradiated tin sphere is presented in Figure 4a. In Figure 4b and 4c, HIM images of the same area before and after 30 keV helium ion irradiation are shown. The irradiation was stopped when clear extrusions appeared. The sample area visible in Figure 4c was imaged by HIM using the minimal necessary fluence (short dwell times and low currents) to not further irradiate the tin spheres during imaging and therefore does not reflect the best possible image quality. The sample was transferred—and thereby exposed to air—to the dual beam tool (Ga FIB, SEM), and the exposed area was identified using SEM imaging. A cross-section has been prepared of several irradiated spheres using Ga-FIB milling. The first milled area is indicated in Figure 4c as a dotted yellow box and the result is presented in Figure 4d. Due to sample tilting towards the FIB column, the sputtered region appears as a trapezoid in the SEM image. Small spheres as shown in Figure 4d show a large cavity in their center. For larger spheres, several smaller He bubbles in a depth corresponding to the projected range of the 30 keV helium beam were observed (not shown here). The sample was further milled, as indicated in Figure 4c by a dashed, red box, and the resulting cross-section is shown in Figure 4e. The sample was rotated clockwise by 45° to be able to look into all three milled structures, and the resulting image is presented in Figure 4f. All cross-sectioned tin spheres which showed crystal-like extrusions have the same kind of cavity like internal structure. We will see later that this finding is essential for the understanding of the observed effect and the proposed model. Very local pre-irradiation of tin spheres creates a hole in the SnO skin and allows to predefine the location of the faceted extrusions which form upon further broad-beam-like irradiation (not shown here). Due to surface sputtering and ion-beam mixing, the oxide layer will be pre-thinned at these locations.

### 3 Modeling, Simulations, and Discussion

The observed ion-irradiation-induced growth of extrusions on tin spheres can be roughly divided into three stages:

- (i) Collisions of the energetic  $\text{He}^+$  ions with tin atoms of the spheres create Frenkel pairs of interstitial atoms and vacancies in the tin lattice. Additionally, such collisions can erode the SnO skin of the tin spheres by sputtering and by ion-beam mixing of the Sn-SnO interface resulting in substoichiometric  $\text{SnO}_x$  ( $x < 1$ ) (**Figure 5a**). As sputtering is strongest for small incident angles (in respect to the surface), the SnO skin becomes damaged most severely near the equator. (ii) With increasing  $\text{He}^+$  ion fluence, the number of deposited He atoms and the number of interstitials and vacancies increases within the tin spheres (Figure 5b). The SnO skin is assumed to be impermeable for He atoms, vacancies, and interstitials [33, 34]. Due to ion erosion of SnO, a contact of the tin core with the external vacuum can form first somewhere along the equator. (iii) Through the hole in the SnO skin, Sn interstitials and vacancies can escape from the core of the tin particle (Figure 5c). As the tin particle is crystalline, the extrusions also become crystalline due to ELO (see e.g. [35]). The only difference to conventional ELO is the source of the atoms: Here, interstitial atoms come from the interior of the spheres through the oxide openings, as compared to atoms delivered by a chemical vapour source. Some of the vacancies capture a helium atom and can therefore not annihilate with an interstitial. In an extreme case, one could consider a situation in which all but one of the interstitial-vacancy pairs—which are created by an incoming  $\text{He}^+$  ion—annihilate. The vacancy of the remaining Frenkel-pair is filled with the implanted helium atom and one interstitial atom per implanted  $\text{He}^+$  ion remains in the lattice. For phosphorus and boron implantation into silicon, this very successful approach is called “+1”-model [36]. The He-filled vacancies diffuse slowly and will unlikely escape through the hole in the SnO skin. They become enriched and form, due to their low nucleation barrier, He nano-bubbles that later coalesce to larger He bubbles within the tin sphere. The creation of helium bubbles was confirmed by FIB cross-sectioning and is observed for other material

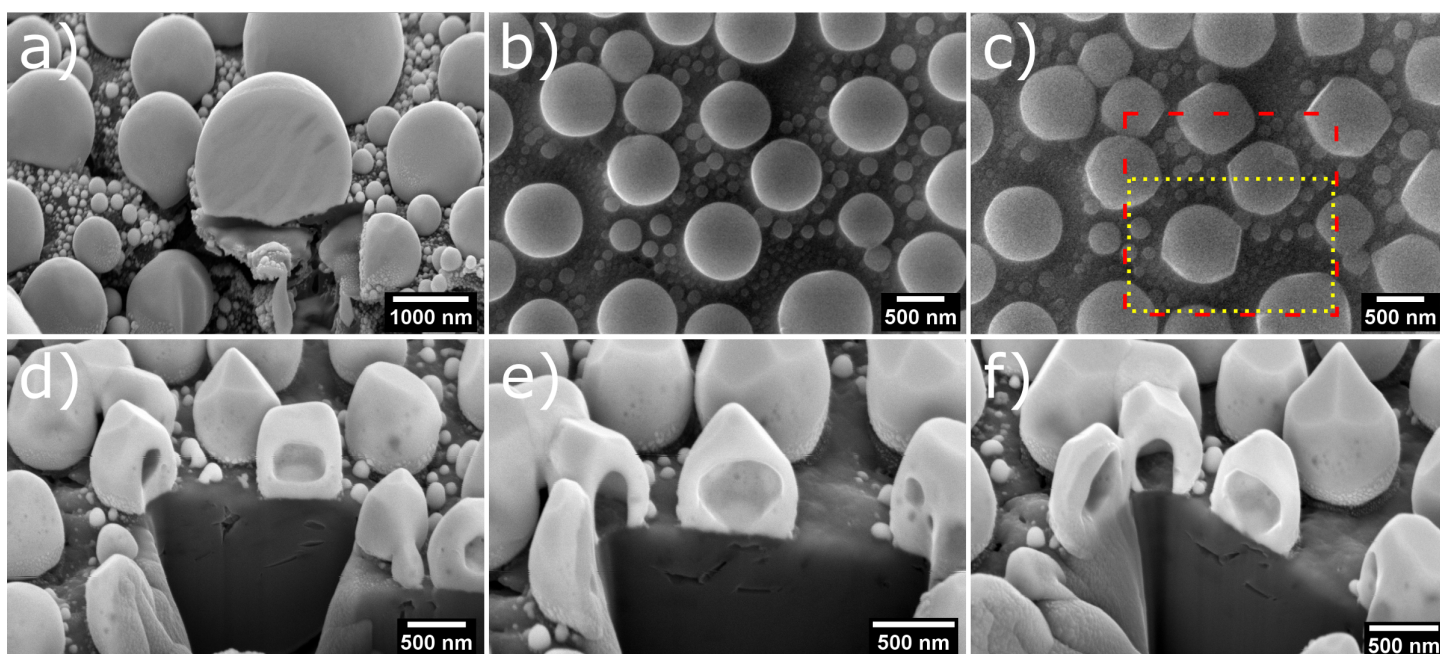


Figure 4: a) SEM image of unirradiated tin spheres. The largest sphere was cut-opened with a gallium FIB. The SEM image was taken at 54° tilt angle. b) to f) show the same area of the sample at various points of the analysis process. b) HIM image before irradiation. c) HIM image after irradiation with visible extrusions. The yellow, dotted rectangle is a guide to the eye indicating the gallium-FIB-milled region shown in 4d. The red, dashed region indicates the milled area visible in 4e and 4f. d) to f) SEM images under 54° tilt of tin spheres with extrusions that were opened by FIB milling. Cavities are visible that were probably filled helium bubbles. In 4f, the sample was rotated clockwise to image the inside of all three opened tin spheres simultaneously.

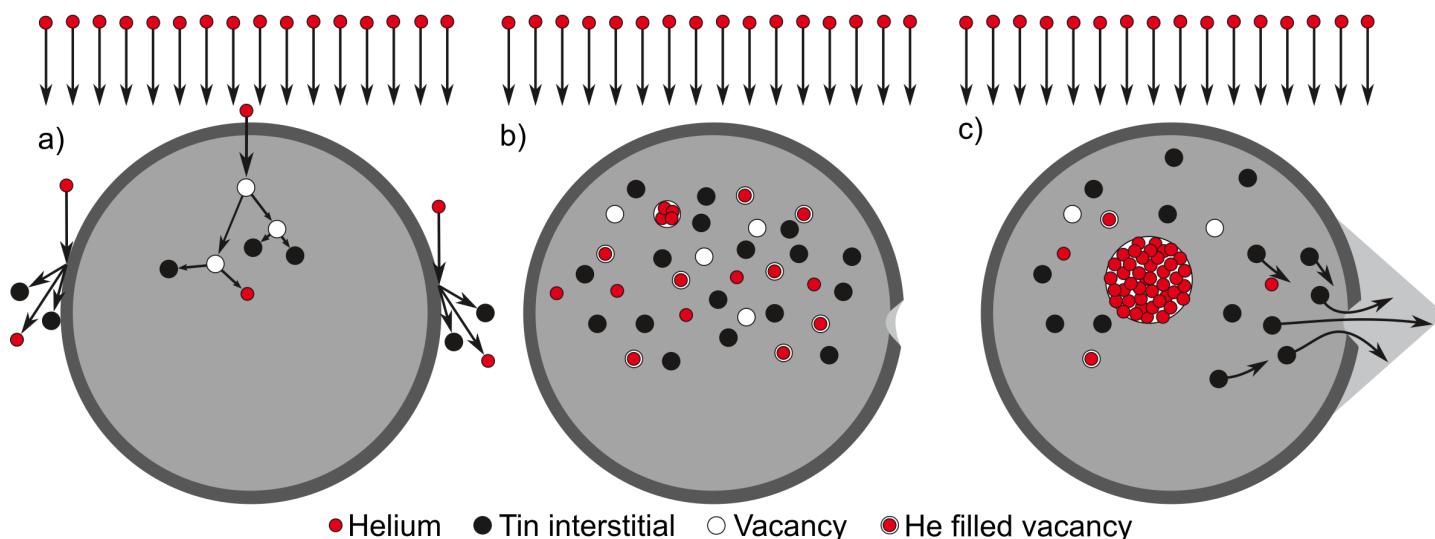


Figure 5: Schematic representation of the proposed model for the formation of extrusions and bubbles in tin micro-spheres. a) Initial state of the irradiation process. Implantation of helium leads directly and also indirectly via the collision cascade to about 70 interstitial-vacancy pairs per implanted ion. About half of the helium is implanted and increased sputtering occurs at the outer edge of the sphere. b) Further implantation leads to increasing helium, interstitial, and vacancy densities. Vacancies can be reoccupied by tin interstitials or filled by helium atoms. Sputter erosion and phase separation will cause somewhere a local exposure of the tin core. c) Epitaxial lateral overgrowth of the tin sphere by escaping tin interstitials and formation of helium bubbles inside the sphere.



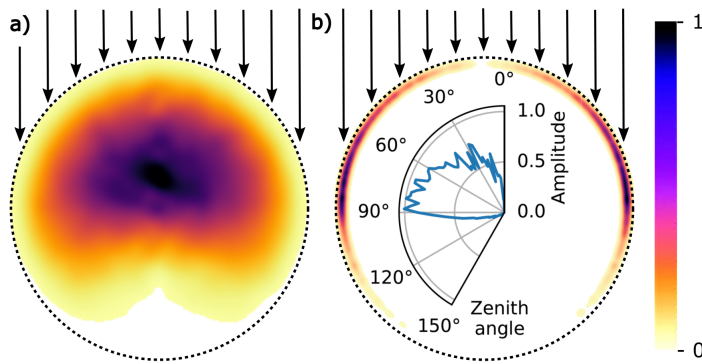


Figure 6: TRI3DST BCA simulation of a nanosphere with 500 nm diameter consisting of a Sn core and a 5 nm tin oxide shell irradiated with 30 keV  $\text{He}^+$ .  $1 \times 10^{10}$   $\text{He}^+$  ion impacts were simulated. a) Normalized  $\text{He}^+$  ion implantation profile, b) normalized sputter ejection profile (thin colored area below the dashed circle). In the inset, the sputter profile of the sphere is plotted in polar coordinates. For angles smaller than  $90^\circ$ , the polar angle also corresponds to the angle of incidence of the ions. For angles larger than  $90^\circ$ , the ions must first enter the sphere and can then sputter particle's from the surface during the projectiles exit. Most particles are sputtered for angles between  $75$  to  $90^\circ$ .

systems, too [8, 9, 13, 37–40].

For stage (i), the spatial distributions of point defects and of implanted  $\text{He}^+$  ions were calculated with the program TRI3DST [41], which is based on the binary collision approximation (BCA). As the projected range ( $156 \pm 70$ ) nm for 30 keV  $\text{He}^+$  ions in tin (simulated with TRIM [42]) is of the order of the size of the tin spheres, a truly three-dimensional program like TRI3DST is indispensable. The simulation of the impact of  $1 \times 10^{10}$   $\text{He}^+$  ions onto a tin sphere of 500 nm diameter having a 5 nm tin oxide skin resulted in an average sputter yield of 0.20 atoms per incident ion and a He deposition efficiency of 49 %. As is evident from the simulation results, 30 keV  $\text{He}^+$  ions become deposited mostly in the upper half of the sphere (**Figure 6a**). For spheres with a diameter smaller than 150 nm, most of the helium will be transmitted and not implanted.

On average, about 70 Frenkel pairs are formed per incoming  $\text{He}^+$  ion, their spatial distribution (calculated also with TRI3DST, but not shown here) is closer to the north pole than the distribution of the implanted He atoms shown in Figure 6a. However, as only one of the interstitials of a Frenkel pair survives, whose nearby vacancy is filled by a He atom, the relevant Sn interstitial generation is approximated by the spatial distribution of implanted He atoms of Figure 6a. Figure 6b

shows that the strongest ion erosion of the tin oxide skin takes place at the equator of the sphere between  $75$  to  $90^\circ$ . There, the  $\text{SnO}$  skin will be removed, as regrowth due to tin oxidation under the used high-vacuum conditions is negligible. Tin extrusions are observed at fluencies slightly above  $2 \times 10^{17}$  ions  $\text{cm}^{-2}$  (see Figure 2b). According to TRI3DST a hole in the  $\text{SnO}$  skin is not yet opened by sputtering. However, besides sputtering, there is ion-beam-induced mixing at the Sn-SnO interface, and the resulting  $\text{SnO}_x$  ( $x < 1$ ) decays into Sn and SnO regions of nm size. Thus, a contact of the tin core with the vacuum can form also without sputtering, just by ion-beam mixing and ion-assisted phase separation of  $\text{SnO}_x$ .

The results of the TRI3DST simulations serve as input data for 3DkMC simulations [43] of the diffusion-reaction kinetics of the He atoms, interstitials, and vacancies. Simulations were performed on a body-centered tetragonal (bct) crystal structure which is close to the A5 lattice structure of  $\beta$ -tin. The A5 structure of  $\beta$ -tin is in fact a double-bct structure [44], which differs energetically only slightly from the simpler bct structure. In our model system, initially, all bct sites inside the sphere are occupied by tin. The sphere is surrounded by a skin of lattice sites which are not reachable by diffusion jumps (dark gray in Figure 5a and green atoms in Figure 7). This skin is a few lattice sites thick and imitates the inert properties of the  $\text{SnO}$  shell with respect to the diffusion [33, 34] of the species considered here. To emulate the holes in the  $\text{SnO}$  formed by sputtering and ion-beam mixing, the  $\text{SnO}$  shell is removed locally at the equator (see Figure 7a), i.e. at this position, tin atoms are in contact with the vacuum. Here, a tin interstitial atom can become a surface adatom and a tin vacancy can become a surface vacancy.

The interatomic interaction of tin atoms is described by a Rosato, Guillopé, and Legrand (RGL) potential [45] fitted to the  $\{200\}$  surface energy and the energy of cohesion of  $\beta$ -tin [46]. Other than in standard Ising-like kinetic Monte Carlo (kMC) simulations, with the RGL potential, the energy of a tin atom is no longer linearly dependent on the number of occupied nearest neighbor sites but shows a square-root-like behavior. Thus, the RGL potential allows a more appropriate description of the kinetics in metals, especially of the formation of the correct crystal facets and the

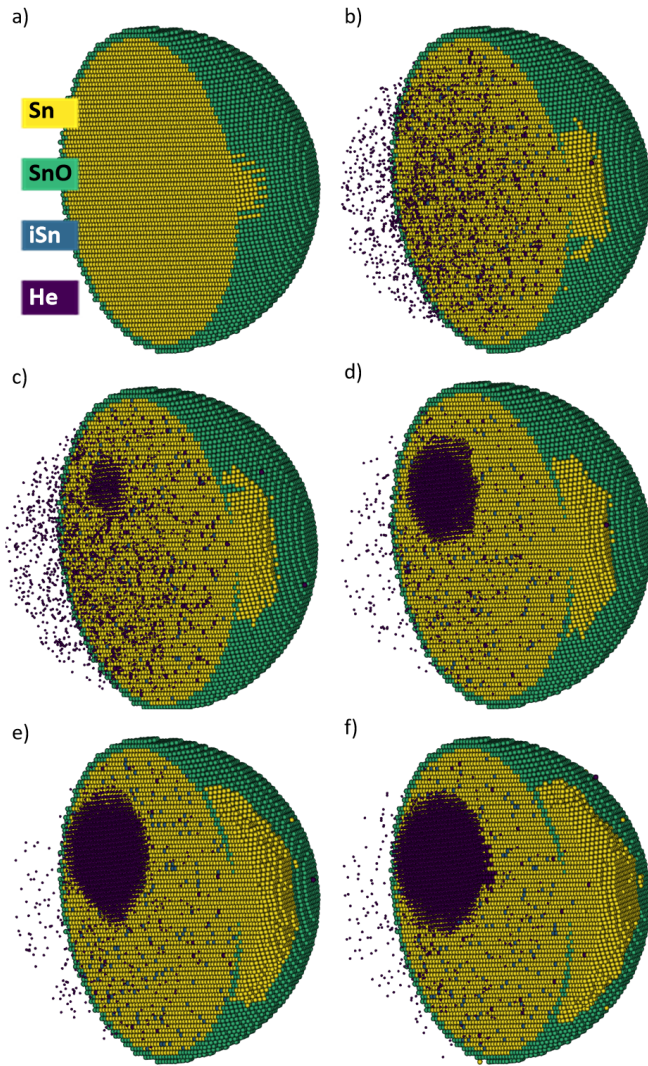


Figure 7: Snapshots of a simulation of  $\text{He}^+$  irradiation of a SnO-covered tin sphere of 500 nm diameter after different equivalent fluencies: To show interior evolution, the spheres are cut in half and all species but He are hidden in one half. Purple points: deposited He atoms, yellow points: bct sites occupied with Sn atoms, green points: SnO species, blue points: Sn atoms on interstitial sites. a) Initial sphere with a hole in the SnO skin. After an equivalent fluence of b)  $4.3 \times 10^{15} \text{ ions cm}^{-2}$ , c)  $5.3 \times 10^{15} \text{ ions cm}^{-2}$ , d)  $6.4 \times 10^{15} \text{ ions cm}^{-2}$ , e)  $1.2 \times 10^{16} \text{ ions cm}^{-2}$ , f)  $1.7 \times 10^{16} \text{ ions cm}^{-2}$ .  $\text{He}^+$  ion is coming from the top, the long axis of the bct lattice is oriented vertically.

nucleation of voids. The interaction of a Sn atom with a SnO species is assumed to depend linearly on the number of nearest neighbor SnO species. This Sn-SnO bond strength is a free parameter in our model. It could be derived from the Sn-SnO interface energy which is unfortunately unknown. Therefore, we modified it until the experimentally found features of extruded tin on the SnO-covered tin sphere were reproduced, resulting in a value of  $1.98 \text{ J m}^{-2}$ . It is assumed that there is no He-Sn nor He-SnO interaction.

The used interatomic tin potential describes suitably the nucleation of voids/He bubbles and the formation of facets on the extrusions as well as at the surface of bubbles. However, the kinetics additionally depends on the migration energy of the species, i.e. the saddle point energy of diffusion jumps. The migration energies of vacancies (empty or He-filled) and tin interstitials could be derived with the Einstein-Smoluchowski equation from their diffusion coefficients which, unfortunately, are not available. It is known, however, that energetic electron irradiation of metals like copper accelerates point-defect-driven microstructure shape changes strongly [18].  $\text{He}^+$  ion irradiation is expected to assist diffusion even more efficiently. Figure 1h shows further evidence for this, as the wetting of the SnO skin is restricted to highly irradiated areas only. Thus, in our model, we implemented the following reasonable approximation which corresponds to the "+1"-model discussed above: From the  $\approx 70$  Frenkel pairs per  $\text{He}^+$  ion impact just one Sn interstitial and one He-filled vacancy survive. For our problem, the validity of the "+1"-model approximation was confirmed by a comparison with a long-lasting 3DlMC simulation taking into account the full generation of 70 Frenkel pairs per He impact (not shown here). A similar assumption on  $\text{He}^+$ -ion-created defects was quite successfully used in the simulation of  $\text{He}^+$  ion irradiation of intermetallic compounds [47]. Possibly more than one He atom can fit into a tin vacancy, this number is a parameter in the 3DlMC simulations. Despite of all the approximations made, the computation time for realistic sphere diameters is prohibitive, thus simulations were carried out for scaled-down spheres, accompanied by also scaling the projected range of the  $\text{He}^+$  ions and the fluence per volume to be equivalent to that of a 500 nm sphere irradiated with  $10^{17} \text{ ions cm}^{-2}$ . Independent of the scaling, the thickness of the SnO



shell is fixed to the minimum value necessary to act as a diffusion barrier. The scaling factor of the sphere diameter in the simulations presented here is roughly 13. Snapshots of a 3DkMC simulation (see Figure 7) show the formation of a faceted tin extrusion on a tin sphere and the formation of a He bubble within the tin sphere. The complete simulated tin sphere evolution under  $\text{He}^+$  ion irradiation is available as a movie in the supplementary material. The extrusion grows epitaxially from the hole in the SnO skin at the equator and overgrows the SnO surface, driven by the tin interstitials diffusing out of the sphere. The He bubbles in the simulation are rhomboidal rather than spherical. Pressure has not been taken into account in our simulations, thus the shapes of the extrusions as well as of the He bubbles are controlled by the surface energies and the point defect kinetics. In longer-running simulations (not shown here) an escape of He bubbles from the interior of the sphere through the extrusion into the vacuum was observed, similar to experimental findings (also not shown here).

## 4 Summary

We report on the effects of high-fluence  $\text{He}^+$  ion implantation into tin spheres within a HIM. The spheres were characterized and analyzed by SEM, XPS, and TEM to be single-crystalline  $\beta$ -tin spheres with a few-nm-thick oxide skin. Under  $\text{He}^+$  irradiation, faceted ELO of tin on the SnO skin starts from holes in the SnO skin, it forms small edged extrusions on the outside of the spheres, which was observed in-situ in the HIM for different irradiation parameters. BCA-based simulations of collision cascades show that high-fluence 30 keV  $\text{He}^+$  irradiation leads to the implantation of nearly half of the supplied helium into a depth of  $\approx 150$  nm below the north poles of 500 nm spheres. In addition, the energetic He particles lead to the creation of  $\approx 70$  Frenkel-pairs per ion and enhanced sputtering of SnO under tangential impact conditions at the equator of the sphere. In the framework of the "+1"-model, for each  $\text{He}^+$  impact, all but one of the Frenkel pairs annihilate due to He occupation of one vacancy, thus one Sn interstitial atom remains. In the course of  $\text{He}^+$  implantation, the helium-vacancy complexes accumulate, He bubbles nucleate and grow. Sn interstitial atoms accumulate too, but due to the increasing

pressure in the SnO-covered tin spheres, the nucleation of Sn dislocations is hampered. Upon creation of an opening in the SnO skin at the equator due to sputtering and ion-beam mixing, the dense Sn interstitial gas can emanate through that hole leading to ELO on the SnO, i.e. the formation of an extrusion. This behaviour was observed experimentally and is qualitatively reproduced by modeling and atomistic simulations of the defect generation and the reaction-diffusion kinetics of the defects. Thus, the observed phenomenon becomes a well-understood mechanism of point-defect-driven nanostructure formation. The  $\text{He}^+$ -irradiation-induced defect generation is intense which allows short experimental studies, and there is a good theoretical understanding of the defect generation. This is quite different for the tin whisker growth which is detrimental for electronics. There, the defect generation rate is very low (and not well understood, e.g. pressure-induced) leading to very long-lasting experiments. Thus, our study of point defect kinetics in tin can help to get a better understanding of tin whisker growth.

As such, the process is not restricted to Sn spheres and He but might also be relevant for many other examples. It is also of importance for a wide range of irradiation conditions that lead to a large numbers of interstitials and where a passivating surface layer prevents the surface from acting as an effective sink for point defects.

## 5 Methods Section

*HIM irradiation:* The ion beam exposure of the tin spheres was performed in a Carl Zeiss NanoFAB using helium and neon ions, the latest generation of HIM devices. Stage- and sample drift were compensated by manually adjusting the irradiation window position and by post-aligning of the recorded image stack using the scale-invariant feature transform algorithm [48] in ImageJ [49]. For the irradiation shown in Figure 1, a primary ion current of  $(6.6 \pm 1.0)$  pA was applied, utilizing a 10  $\mu\text{m}$  aperture,  $5.2 \times 10^{-6}$  mbar helium gas pressure in the ion source, and a crossover position of  $-193$  mm (spotcontrol 3). The dwell time per pixel was chosen to be 10  $\mu\text{s}$ , capturing  $(512 \times 512)$  pixel images on a FOV of 2.0  $\mu\text{m}$ . This equals to 2.6 s irradiation time per image, a fluence of  $2.7 \times 10^{15}$  ions  $\text{cm}^{-2}$  per scan, and a flux of  $1 \times 10^{15}$  ions  $\text{cm}^{-2} \text{s}^{-1}$ . After 301 im-

ages, the resulting total implantation fluence was  $8.3 \times 10^{17}$  ions  $\text{cm}^{-2}$ , resulting in a total irradiation time of approximately 13 min. The chamber pressure during the irradiation was below  $2.0 \times 10^{-7}$  mbar.

The irradiation shown in Figure 2 was performed with  $(0.2 \pm 0.1)$  pA of 30 keV  $\text{He}^+$  using a 10  $\mu\text{m}$  aperture,  $4.5 \times 10^{-6}$  mbar helium gas pressure in the ion source, and a crossover position of  $-246$  mm (spotcontrol 6). The dwell time per pixel was chosen to be 5  $\mu\text{s}$  capturing  $(1024 \times 1024)$  pixel images at a FOV of 2.0  $\mu\text{m}$ , while every scan line was averaged 4 times. With an irradiation time per image of 21 s and a fluence of  $7.3 \times 10^{14}$  ions  $\text{cm}^{-2}$  per scan, we calculate a flux of  $3.5 \times 10^{13}$  ions  $\text{cm}^{-2} \text{s}^{-1}$ . 521 images equal a total irradiation fluence of  $3.8 \times 10^{17}$  ions  $\text{cm}^{-2}$  and a total irradiation time of 3 h. Including the time for saving the individual images and correction for drift, the irradiation was done in 9 h in total, split in two sessions.

In Figure 3d, a tin sphere is shown that was irradiated with 2.0 pA of 30 keV  $\text{He}^+$  by using a 10  $\mu\text{m}$  aperture,  $5.6 \times 10^{-6}$  mbar helium gas pressure in the ion source, and a crossover position of  $-229$  mm (spotcontrol 5). 5  $\mu\text{s}$  dwell time per pixel was used to capture  $(1024 \times 1024)$  pixel images on a FOV of 1.4  $\mu\text{m}$  without line averaging. The irradiation time per image was 5.2 s, resulting in a fluence of  $3.3 \times 10^{15}$  ions  $\text{cm}^{-2}$  per scan and a flux of  $6.4 \times 10^{14}$  ions  $\text{cm}^{-2} \text{s}^{-1}$ . 71 image scans equal to a total implantation fluence of  $2.4 \times 10^{17}$  ions  $\text{cm}^{-2}$ . A video of the irradiation process can be found in the supplementary information.

**TEM and SEM analysis:** Smaller tin spheres were analyzed by TEM. Selected-area electron diffraction (SAED) and high-resolution transmission electron microscopy (HRTEM) imaging were performed with an image- $\text{C}_s$ -corrected Titan 80-300 microscope (FEI) operated at an accelerating voltage of 300 kV. Additionally, spectrum imaging analysis based on energy-dispersive X-ray spectroscopy (EDXS) was done in scanning transmission electron microscopy (STEM) mode at 200 kV with a Talos F200X microscope equipped with a Super-X EDX detector system (FEI). XPS measurements have been performed using a Microlab 310-F from Thermo Scientific. A Zeiss NVision 40 CrossBeam Workstation was used to perform Ga FIB cross-sectioning and SEM imaging.

## 6 Supporting Information

Supporting Information is available from the Wiley Online Library, from the author or RODARE (TODO).

## 7 Acknowledgements

This research was carried out at the Ion Beam Center (IBC) at the Helmholtz-Zentrum Dresden—Rossendorf e. V., a member of the Helmholtz Association.

## 8 Conflict of Interest

The authors declare no conflict of interest.

## 9 Author Contributions

NK performed HIM experiments. KHH did modeling and DT performed 3DkMC simulations. WM delivered BCA simulations. RH carried out all TEM-based experiments. LB did FIB cross-sections. SF was responsible for XPS analysis. KHH, WM, NK and GH developed the theoretical model. All authors contributed to the data analysis and co-wrote the manuscript.

## 10 Data Availability Statement

The data that support the findings of this study are available from the corresponding author upon reasonable request.

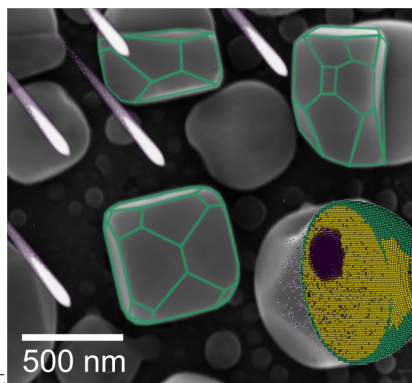
## References

- [1] N. Furuta, K. Hamamura, *Japanese Journal of Applied Physics* **1969**, *8*, 12 1404.
- [2] G. Galyon, *IEEE Transactions on Electronics Packaging Manufacturing* **2005**, *28*, 1 94.
- [3] J. B. LeBret, M. G. Norton, *Journal of Materials Research* **2003**, *18*, 3 585.
- [4] N. A. Fadil, S. Z. Yusof, T. A. A. Bakar, H. Ghazali, M. A. M. Yajid, S. A. Osman, A. Ourdjini, *Materials* **2021**, *14*, 22 6817.
- [5] S. H. Liu, C. Chen, P. C. Liu, T. Chou, *Journal of Applied Physics* **2004**, *95*, 12 7742.

- [6] J. Smetana, IEEE Transactions on Electronics Packaging Manufacturing **2007**, 30, 1 11.
- [7] N. Jain, X. Wang, P. Jagtap, A. Bower, E. Chason, Journal of Electronic Materials **2021**, 50, 12 6639.
- [8] R. Livengood, S. Tan, Y. Greenzweig, J. Notte, S. McVey, Journal of Vacuum Science & Technology B: Microelectronics and Nanometer Structures **2009**, 27, 6 3244.
- [9] V. Veligura, G. Hlawacek, R. P. Berkeelaar, R. van Gastel, H. J. W. Zandvliet, B. Poelsema, Beilstein Journal of Nanotechnology **2013**, 4 453.
- [10] F. Bergner, G. Hlawacek, C. Heintze, J. Nucl. Mater. **2017**.
- [11] G. Shan, Y. Chen, N. Liang, H. Dong, W. Zhang, T. Suo, F. Liu, Materials Letters **2019**, 238 261.
- [12] F. I. Allen, P. Hosemann, M. Balooch, Scr. Mater. **2020**, 178 256.
- [13] Z.-J. Wang, F. I. Allen, Z.-W. Shan, P. Hosemann, Acta Materialia **2016**, 121 78.
- [14] H. Bolt, V. Barabash, G. Federici, J. Linke, A. Loarte, J. Roth, K. Sato, J. Nucl. Mater. **2002**, 307-311, 1 SUPPL. 43.
- [15] E. Snoeks, A. Van Blaaderen, T. Van Dillen, C. M. Van Kats, K. Velikov, M. L. Brongersma, A. Polman, Nuclear Instruments and Methods in Physics Research, Section B: Beam Interactions with Materials and Atoms **2001**, 178, 1-4 62.
- [16] B. Schmidt, K.-H. Heinig, A. Mücklich, C. Akhmadaliev, Nuclear Instruments and Methods in Physics Research Section B: Beam Interactions with Materials and Atoms **2009**, 267, 8-9 1345.
- [17] X. Xu, K.-H. Heinig, W. Möller, H.-J. Engelmann, N. Klingner, A. Gharbi, R. Tiron, J. von Borany, G. Hlawacek, Semiconductor Science and Technology **2020**, 35, 1 015021.
- [18] M. E. Toimil-Molares, L. Röntzsch, W. Sigle, K.-H. Heinig, C. Trautmann, R. Neumann, Advanced Functional Materials **2012**, 22, 4 695.
- [19] K. R. Carson, M. L. Rudee, J. Sci. Instrum. **1967**, 44, 12 1036.
- [20] Tedpella, 600, tin spheres on carbon, low magnification, URL [https://www.tedpella.com/calibration\\_html/SEM\\_Resolution\\_Test\\_Specimens\\_Tin\\_on\\_Carbon.htm#600](https://www.tedpella.com/calibration_html/SEM_Resolution_Test_Specimens_Tin_on_Carbon.htm#600).
- [21] Emdiasum, 79518-01, tin-c low mag test specimen on 12.5 mm pin stub, URL [https://www.emsdiasum.com/microscopy/products/calibration/sem\\_resolution.aspx#79515](https://www.emsdiasum.com/microscopy/products/calibration/sem_resolution.aspx#79515).
- [22] Spi, 02863-ab, spi supplies tin on carbon sem image resolution checker specimen, URL <https://www.2spi.com/item/02863-ab/sem-tin-carbon/>.
- [23] Plano, S1937, Universal-Testobjekt - Zinn auf Kohle (REM Sn-C, Teilchengröße < 5 nm - 30  $\mu$ m), URL <https://www.plano-em.de/testobjekte/zinn-auf-kohle-universal?number=S1937>.
- [24] B. W. Ward, J. A. Notte, N. P. Economou, Journal of Vacuum Science & Technology B: Microelectronics and Nanometer Structures **2006**, 24, 6 2871.
- [25] J. A. Notte, R. Hill, B. W. Ward, N. P. Economou, R. Hill, R. Percival, L. Farkas, S. McVey, AIP Conf. Proc. **2007**, 931, 4 489.
- [26] G. Hlawacek, V. Veligura, R. van Gastel, B. Poelsema, Journal of Vacuum Science & Technology B: Microelectronics and Nanometer Structures **2014**, 32, 2 020801.
- [27] G. Hlawacek, A. Götzhäuser, editors, Helium Ion Microscopy, Springer International Publishing, **2016**.
- [28] N. Klingner, R. Heller, G. Hlawacek, J. von Borany, J. Notte, J. Huang, S. Facsko, Ultramicroscopy **2016**, 162 91.
- [29] N. Klingner, R. Heller, G. Hlawacek, S. Facsko, J. von Borany, Ultramicroscopy **2019**, 198 10.
- [30] C. P. Mauer, Kalman Filter, <https://imagej.nih.gov/ij/plugins/kalman.html>, URL <https://imagej.nih.gov/ij/plugins/kalman.html>.
- [31] J. F. Ziegler, M. Ziegler, J. Biersack, Nuclear Instruments and Methods in Physics Research Section B: Beam Interactions with Materials and Atoms **2010**, 268, 11-12 1818.

- [32] J. Leitner, D. Sedmidubský, volume 40. Springer Science and Business Media LLC, **2018** 10–20.
- [33] K. N. Tu, Physical Review B **1994**, 49, 3 2030.
- [34] A. Togo, F. Oba, I. Tanaka, K. Tatsumi, volume 74. American Physical Society (APS), **2006** 195128.
- [35] S.-H. Kim, S. H. Lee, J.-W. Park, T. M. Roh, D. Suh, Applied Materials Today **2021**, 24 101143.
- [36] M. D. Giles, J Electrochem Soc **1991**, 138, 4 1160.
- [37] W. D. Wilson, M. I. Baskes, C. L. Bisson, Physical Review B **1976**, 13, 6 2470.
- [38] J. Evans, J. Nucl. Mater. **1978**, 76-77 228.
- [39] H. Trinkaus, Radiation Effects **1983**, 78, 1-4 189.
- [40] S. E. Donnelly, Radiat. Eff. **1985**, 90, 1-2 1.
- [41] M. L. Nietiadi, L. Sandoval, H. M. Urbassek, W. Möller, Phys. Rev. B **2014**, 90, 4 045417.
- [42] J. F. Ziegler, J. P. Biersack, M. D. Ziegler, SRIM - The Stopping and Range of Ions in Matter, **2008**.
- [43] M. Strobel, K.-H. Heinig, W. Möller, Physical Review B **2001**, 64, 24 245422.
- [44] D. Mukherjee, K. D. Joshi, S. C. Gupta, Journal of Physics: Conference Series **2010**, 215 012106.
- [45] V. Rosato, M. Guillope, B. Legrand, Philosophical Magazine A **1989**, 59, 2 321.
- [46] P. Eckold, M. Sellers, R. Niewa, W. HÜgel, Microelectron Reliab **2015**, 55, 12 2799.
- [47] H. Bernas, J.-P. Attané, K.-H. Heinig, D. Halley, D. Ravelosona, A. Marty, P. Auric, C. Chappert, Y. Samson, Physical Review Letters **2003**, 91, 7 077203.
- [48] D. G. Lowe, Int J Comput Vision **2004**, 60, 2 91.
- [49] C. A. Schneider, W. S. Rasband, K. W. Eliceiri, Nature Methods **2012**, 9, 7 671.

Table of Contents



Helium ion implantation into tin spheres results in an interstitial excess leading to epitaxial overgrowth. The shown approach enables initiation and in-situ direct observation of interstitial-driven effects that can contribute to the understanding of whisker growth in lead-free solder. Modeling and simulation of the experimentally observed morphologies allows an estimation of the tin and tin oxide surface boundary energy.